Electronic Supplementary Information (ESI)

Additive engineering strategies for improved interfacial stability in lithium metal batteries

Kun Ryu,‡[a,b] Kyungbin Lee,‡[a] Jeonghoon Lim,[c] Michael J. Lee,[a] Keun-Hee Kim,[a] Un Hwan Lee,[d] Bernardine Rinkel,[c] Kyungmo Kim,[a] Soohyun Kim,[e] Dayoung Kim,[e] Dongsek Shin,[e] Bryan McCloskey,[c] Joonhee Kang,[d*] and Seung Woo Lee[a*]

[a]George W. Woodruff School of Mechanical Engineering, Georgia Institute of Technology, Atlanta, GA, 30332, USA.

[b]Pritzker School of Molecular Engineering, University of Chicago, Chicago, IL, 60637, USA.

[c]Department of Chemical and Biomolecular Engineering, University of California, Berkeley, CA, 94720, USA.

[d]Department of Nanoenergy Engineering, Pusan National University, Busan, 46241, Republic of Korea.

[e]LG Energy Solution, Ltd., LG Science Park, Seoul 07796, Korea

Co-correspondence: seung.lee@me.gatech.edu, j.kang@pusan.ac.kr

Supplementary Experimental Section

Electrolyte and electrode preparation

For the ether electrolytes, 1M lithium bis(fluorosulfonyl)imide (LiFSI, Solvionic) was dissolved in anhydrous tetrahydrofuran (THF, Sigma-Aldrich). Tetrabutylammonium tetrafluoroborate (TBATFB, Sigma-Aldrich) were processed using the following protocols to remove any excess water. After vacuum drying in 80 ˚C for 48 hours, TBATFB was dissolved in THF and then refluxed in Argon environment for 2 hours. The salt was subsequently recrystallized in anhydrous ethyl acetate (Sigma-Aldrich) to obtain white crystals. Then, 0.1 M, 0.5 M, and 1.0 M concentrations of TBATFB were added to the 1 M LiFSI/THF electrolytes. The $LiFePO_4$ (LFP, MSE Supplies) and single crystal $LiNi_{0.88}Co_{0.09}Al_{0.03}O_2$ (NCA-88, MSE Supplies) cathodes were prepared using a slurry cast method. Initially, a slurry was created by mixing the active material, Super P carbon black, and Polyvinylidene fluoride (PVDF) binder (MSE Supplies) in a mass ratio of 90:5:5 in anhydrous N-methyl pyrrolidone (NMP, Sigma-Aldrich). The slurry was then casted using a doctor blade method onto aluminium foil and punched into 13 mm disks. Subsequently. the cathodes were pressed with roll press at 90 °C. The electrodes underwent vacuum drying for at least 24 hours at 65 °C prior to cell assembly.

Electrochemical Characterization

All tests were conducted using 2032-type coin cells assembled in an Argon-filled glovebox (MBRAUN, O_2 and H_2O < 0.1 ppm) with polypropylene (Celgard 2325) as the separator. Li||Li symmetric cells and Li||Cu asymmetric cells were assembled using a 250 μm Li chip as the reference and counter electrode. The exchange current density was determined using the Tafel plot and the Butler-Volmer equation. To generate a Tafel plot, the Li||Li cell was scanned at a constant rate of 0.5 mV s^{-1} within a voltage range of -0.2 and 0.2 V vs. Li/Li^+. The overpotentials needed

for the Butler-Volmer equations were obtained through galvanostatic charge/discharge of Li||Li cells, using currents ranging from 20 to 100 μA. The passivation stability of the Li metal anode was assessed by setting up a Li||Cu cell at 0 V vs. Li/Li^+ and monitoring the leakage current for 10 hours. Calendar ageing of Li was performed by initially plating and stripping 5 mAh cm^{-2} of Li, followed by another plating 5 mAh cm^{-2} of Li. The cells were then allowed to rest for 0, 1, and 5 days before being stripped to 1 V vs. Li/Li^+. Li||LFP full cell batteries were tested using a 35-μm-thick Li anode and a 4 mAh cm^{-2} loading LFP cathode, within a voltage range of 2.5 – 4.0 V vs. Li/Li^+. Li||NCA-88 full-cell batteries were tested using either a 35-μm-thick or 50-μm-thick Li anode, coupled with a 2 mAh cm^{-2} or 4 mAh cm^{-2} NCA-88 cathode, within the voltage range of 2.7 – 4.3 V vs. Li/Li^+. Anode-free Cu||NCA-88 cells were assembled using Cu foil as the anode and a 2 mAh cm^{-2} NCA-88 cathode within the same voltage range. Electrochemical floating test was performed by placing a Li||NCA-88 cell at 4.3 V vs. Li/Li^+ and measuring the leakage current. Galvanostatic Intermittent Titration Technique (GITT) was performed by charging and discharging at 0.02 C with 45-minute rest intervals. Electrochemical impedance spectroscopy (EIS) experiments were carried out from 10^{-2} Hz to 10^5 Hz using a 10-mV peak voltage at open-circuit voltage. The ionic conductivity and transference number of the electrolytes were measured using EIS with SS||SS and Li||Li symmetric cells, respectively. The transference number was determined using the Bruce-Vincent method with a polarization voltage and time of 10 mV and 2 hours. Identical conditions were used for measuring the total impedance of Li||Li and Li||NCA-88 full cells. BioLogic VMP3 and Arbin battery cyclers were used for all electrochemical analysis.

Materials Characterization

The morphology of the Li metal deposits was examined using scanning electron microscopy (SEM, SU-8230). The electrolyte's solvation structure was analyzed using Raman Spectroscopy

(Renishaw Qontor Dispersive Raman Spectrometer). The chemical composition of the SEI and CEI was investigated using X-ray photoelectron spectroscopy (Thermo Scientific K-alpha XPS instrument) with air-tight transfer. High-resolution XPS of Li 1s, C 1s, O 1s, F 1s, and S 2p spectra were fitted using XPSPEAKS 4.1. One-dimensional ^{7}Li, $^{19}F\{^{1}H\}$ and ^{17}O NMR spectra were recorded on a Bruker AVANCE III HD 14.1 T (ω_{1H} = 600 MHz) spectrometer using a BB Prodigy CryoProbe. All spectra were internally referenced by adding a glass capillary containing an appropriate reference solution: ^{7}Li NMR spectra were referenced to LiCl (1 M in D_2O) at 0.0 ppm, ^{19}F NMR spectra were referenced to $LiPF_6$ (1 M in EC/DMC; 1:1 v/v) at −74.5 ppm (δ ^{19}F), and ^{17}O spectra were referenced to D_2O at 0.0 ppm.

Computational Details

We employed the Vienna ab-initio simulation package (VASP) for conducting density functional theory (DFT) computations.[1,2] The projector augmented wave (PAW) approach was utilized for core electron representation,[3] and the determination of the exchange-correlation functional relied on the Perdew-Burke-Ernzerhof (PBE) method within the framework of the generalized gradient approximation (GGA).[4] We selected a plane-wave cutoff energy of 400 eV and enforced an energy convergence threshold of 10^{-5} eV, continuing computations until atomic forces diminished to below 0.02 eV $Å^{-1}$. For the optimization of molecular adsorption structures, we integrated the Brillouin zone in reciprocal space using a 1 × 1 × 1 k-point grid, and we also utilized a 1 × 1 × 1 k-point grid for ab-initio molecular dynamics (AIMD) calculations to enhance computational speed. Spin polarization was considered in all calculations except for AIMD simulations. The Li (100) surface was modeled with a 6 × 6 supercell containing 3 layers, with the bottom two layers fixed to represent the bulk region. For surface AIMD calculations, we performed 50,000 steps with a time step of 1 fs under the condition of 300K temperature. To prevent interactions due to periodic

boundary conditions during relaxations involving molecules and surfaces, a vacuum of at least 15 Å was included. For computing solvation structures in the electrolytes, we employed the universal graph deep learning interatomic potential (M3GNet) for fast computations.[5] The conventional ether electrolyte (CEE) was modeled with 5 LiFSI and 60 THF molecules, while the additive-containing electrolyte (ACE) included an additional TBATFB in addition to CEE. Molecular dynamics simulations for observing electrolyte solvation structures were performed for 30 ps at a temperature of 350 K.

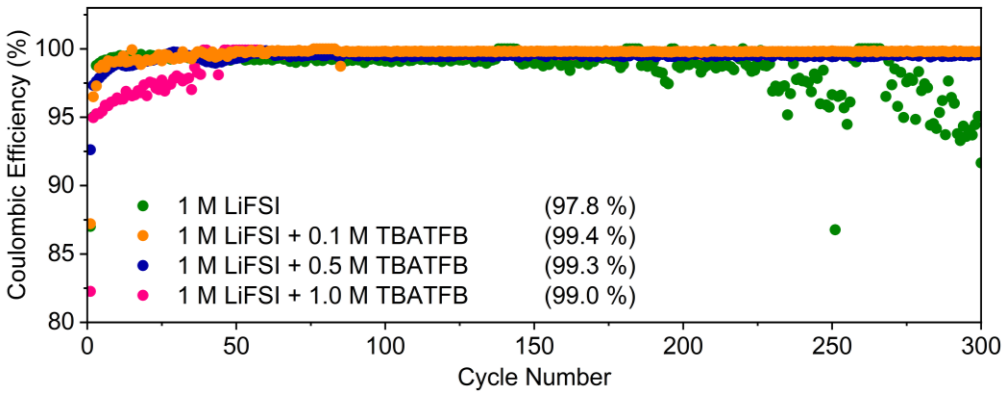

Fig. S1. Li plating/stripping CEs for Li||Cu asymmetric cells at 1 mA cm^{-2} and 1 mAh cm^{-2}.

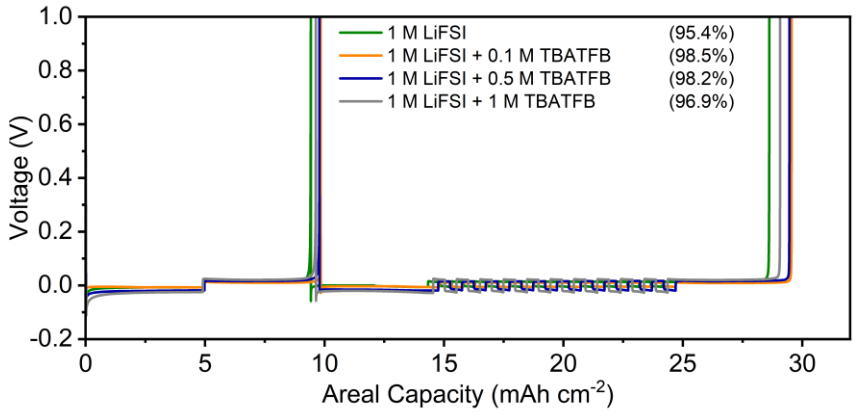

Fig. S2. Li plating/stripping protocol for Li||Cu asymmetric cells at 0.5 mA cm^{-2} and 5 mAh cm^{-2}.

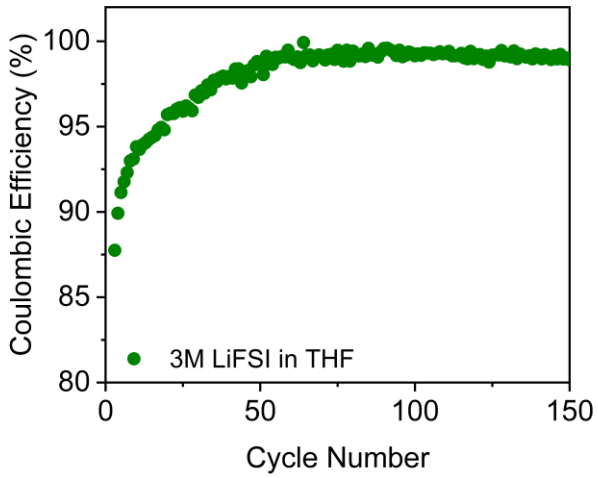

Fig. S3. Li plating/stripping CEs for the Li||Cu asymmetric cell using a high-concentration electrolyte of 3 M LiFSI in THF at 1 mA cm^{-2} and 1 mAh cm^{-2}.

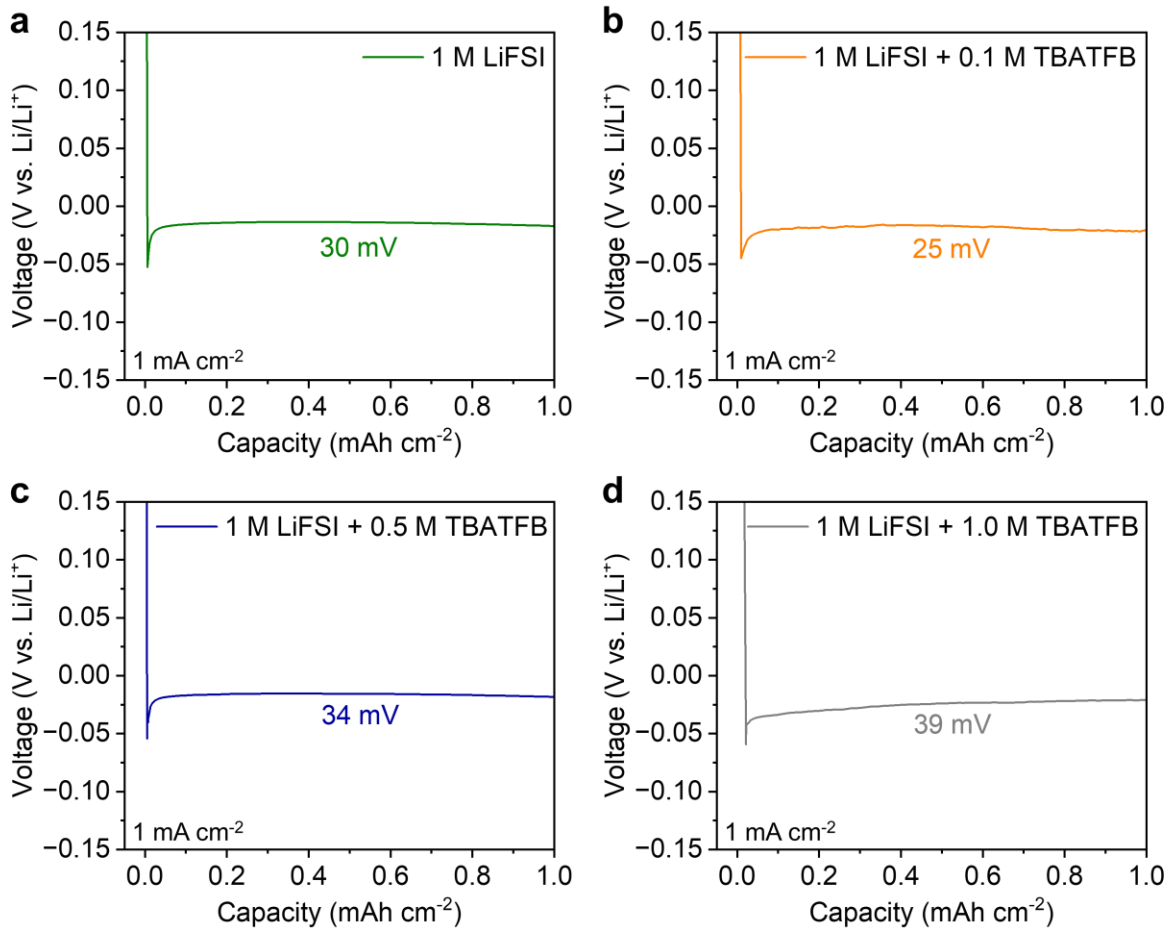

Fig. S4. Nucleation overpotential profiles of different electrolytes at current density of 1 mA cm^{-2}.

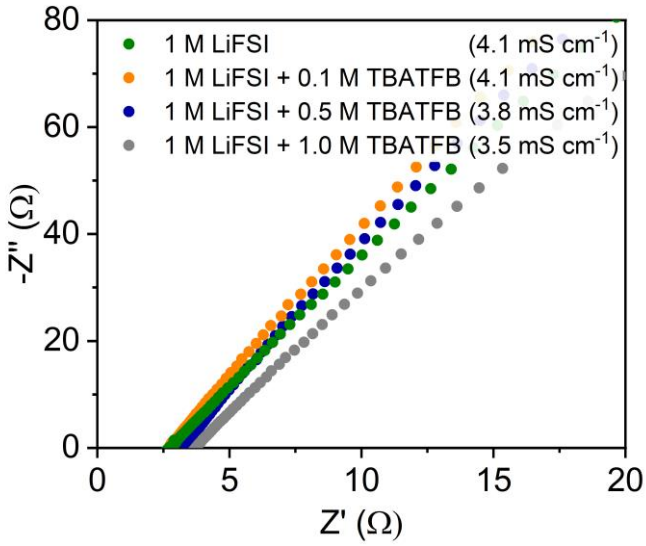

Fig. S5. Ionic conductivity measurements of different electrolytes.

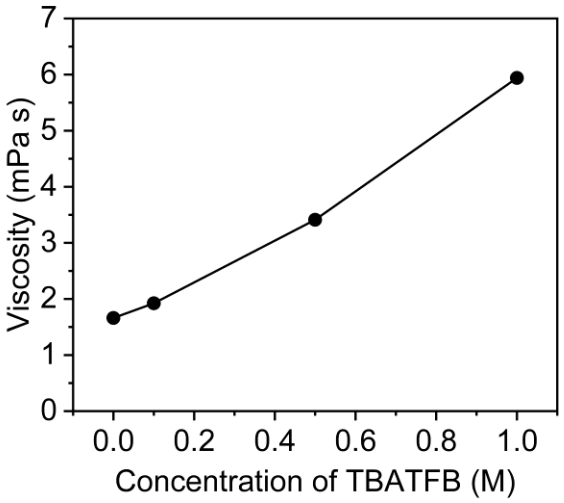

Fig. S6. Viscosity of different electrolytes measured as a function of TBATFB concentration in 1M LiFSI in THF.

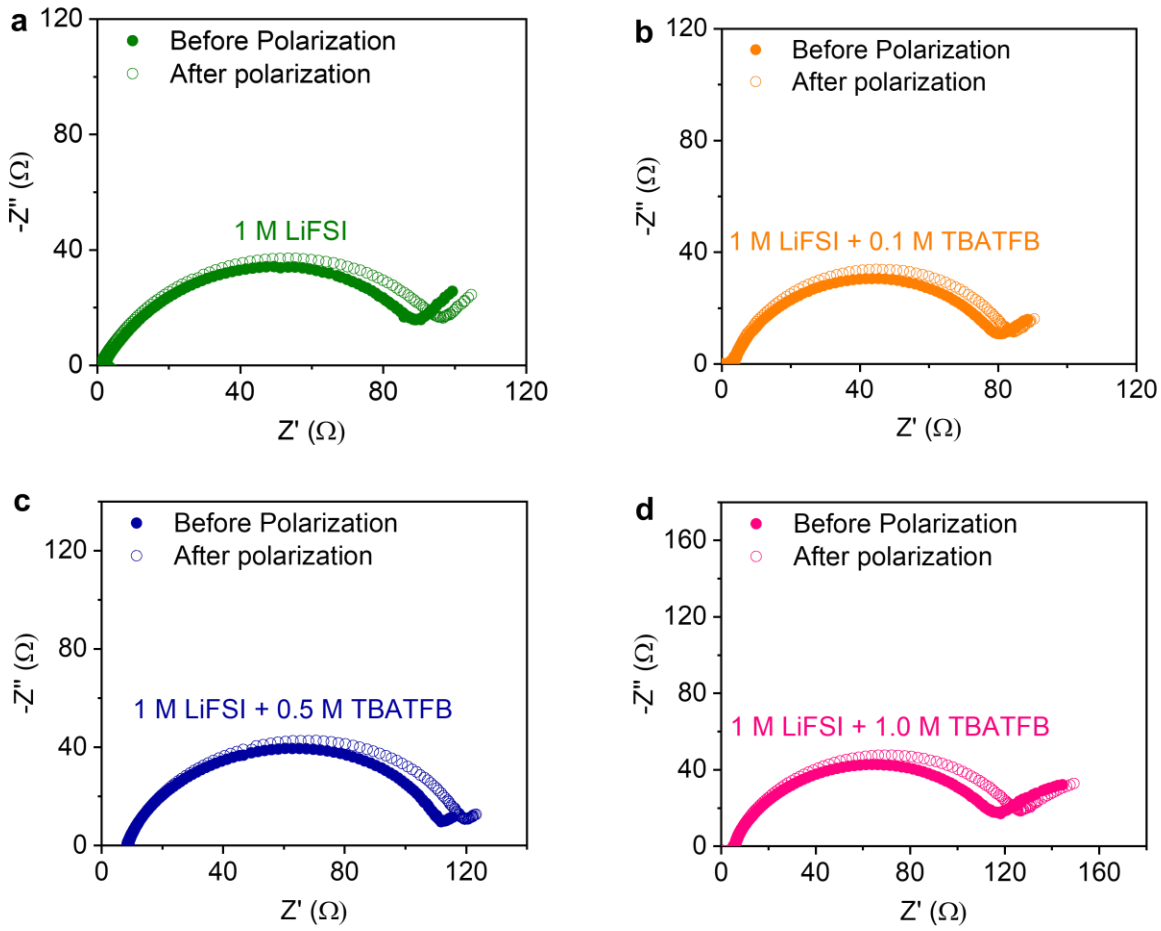

Fig. S7. Nyquist plots of Li||Li symmetric cells before and after polarization of 10 mV.

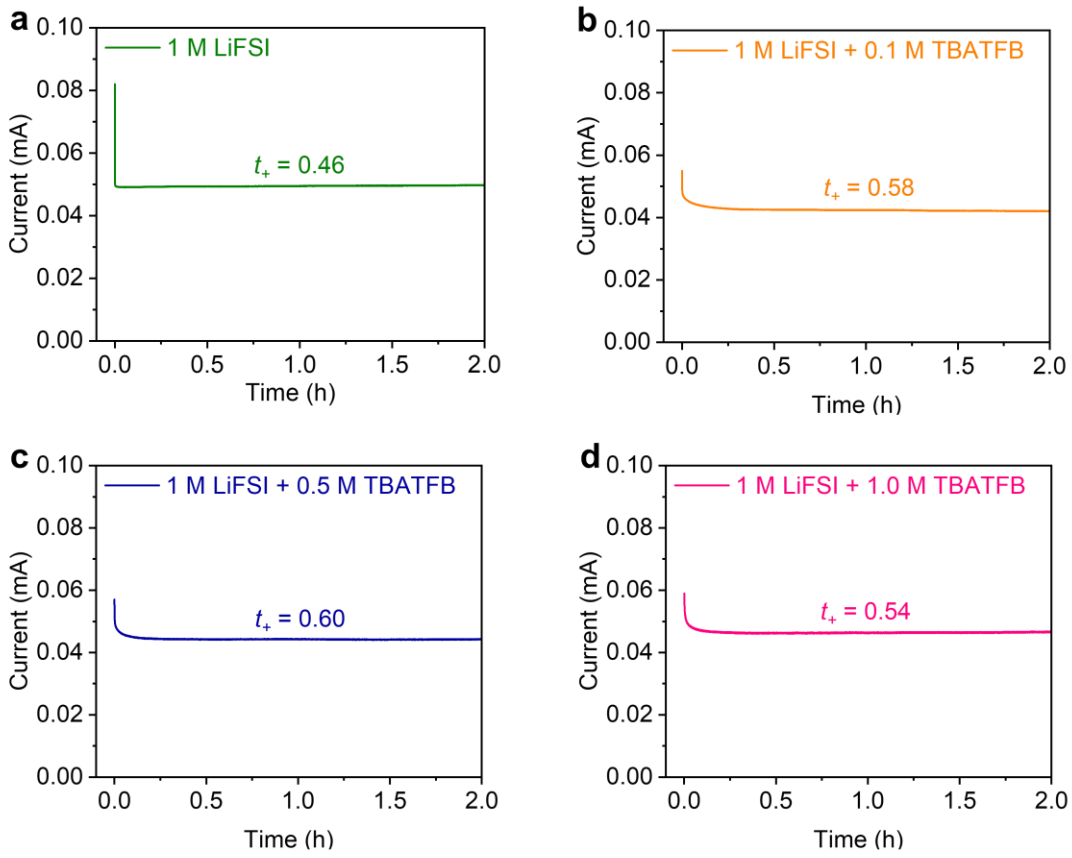

Fig. S8. Steady state current measurement of Li||Li symmetric cells under 10 mV for 2 hours.

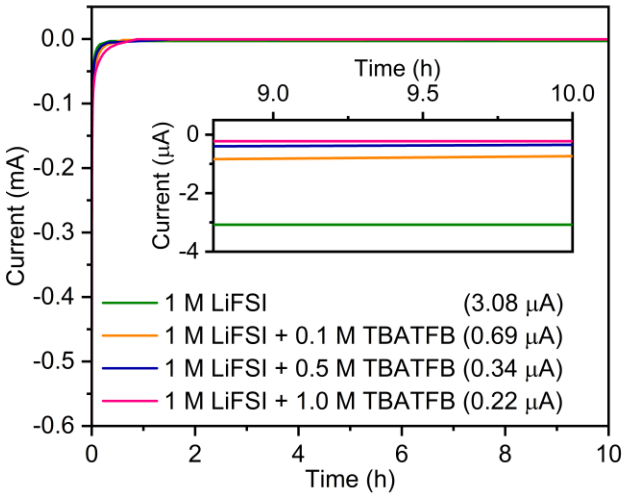

Fig. S9. Passivation leakage current measurement of Li||Cu cells at 0 V vs. Li/Li^+ for 10 hours.

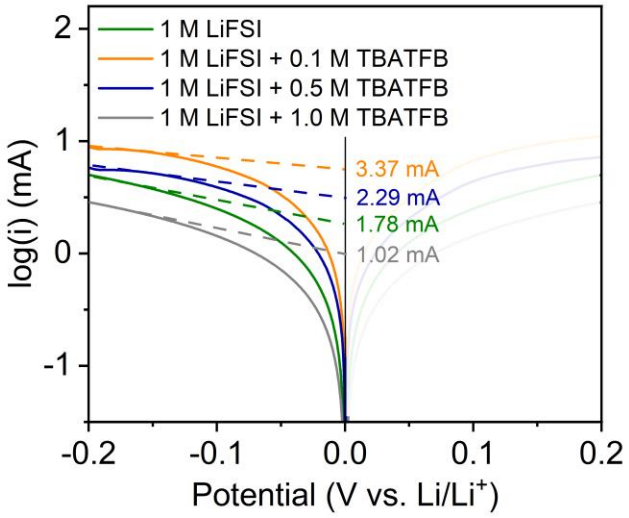

Fig. S10. Tafel plot of Li||Li symmetric cells measured between - 0.2 and 0.2 V vs. Li/Li^+ under scan rate of 0.5 mV s^{-1}.

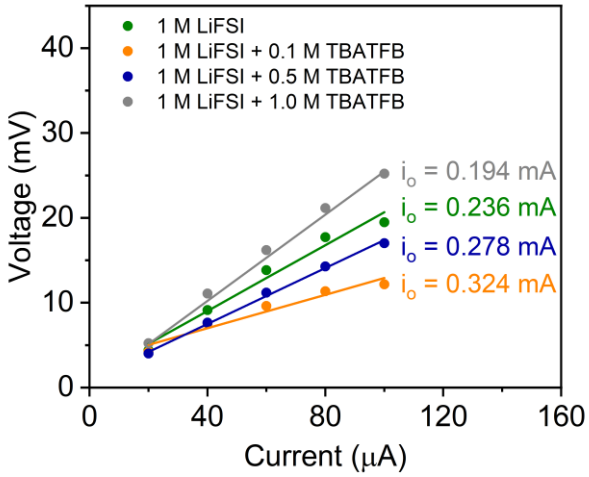

Fig. S11. Overpotentials of galvanostatic charge/discharge cycles under low currents, ranging from 20 to 100 μA.

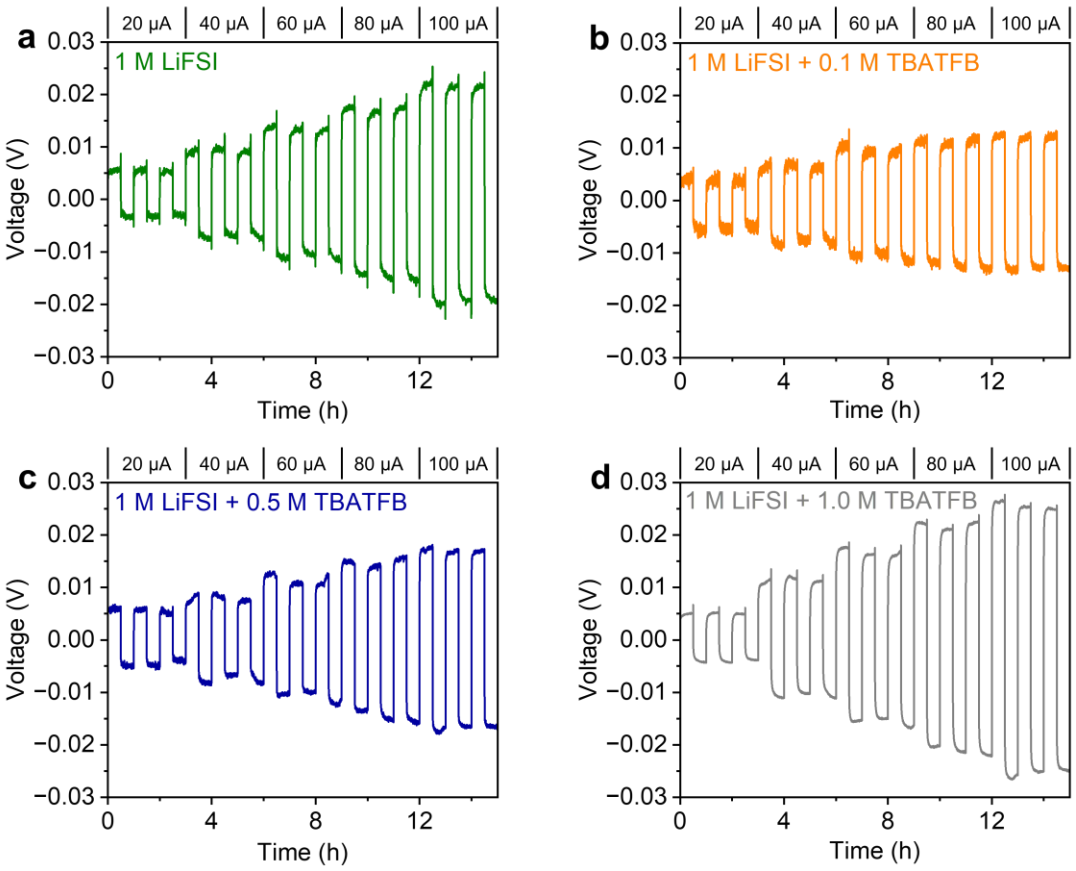

Fig. S12. Voltage profiles of galvanostatic charge/discharge under low currents, ranging from 20 to 100 μA.

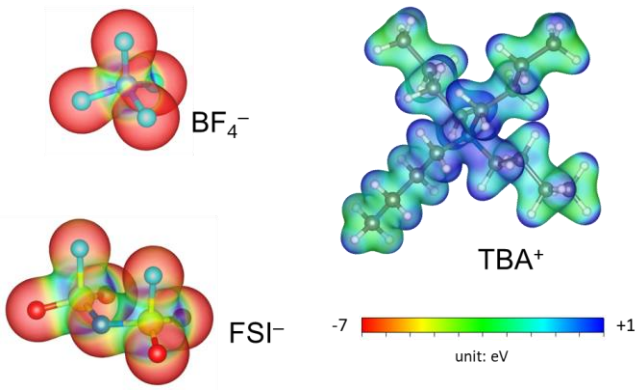

Fig. S13. Electrostatic potential of BF_4^-, FSI^-, and TBA^+ ions calculated using density functional theory (DFT).

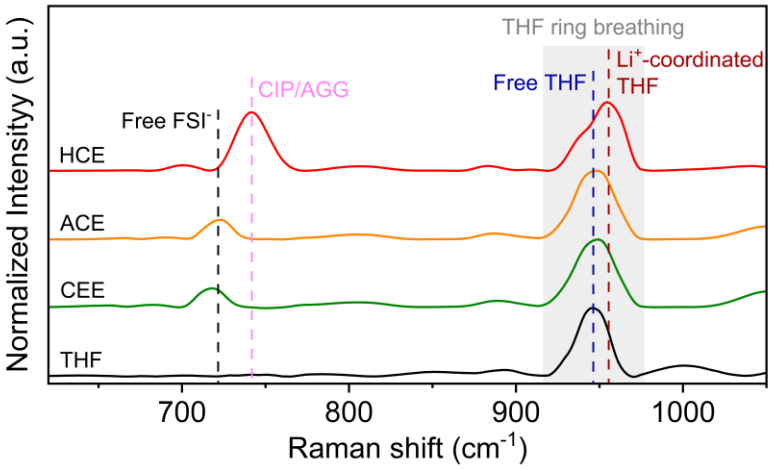

Fig. S14. Raman spectra of pure THF, CEE, ACE, and high-concentration electrolyte (HCE, 3 M LiFSI in THF). HCE was added to show a clear difference between the free FSI^-/THF and coordinated FSI^-/THF.

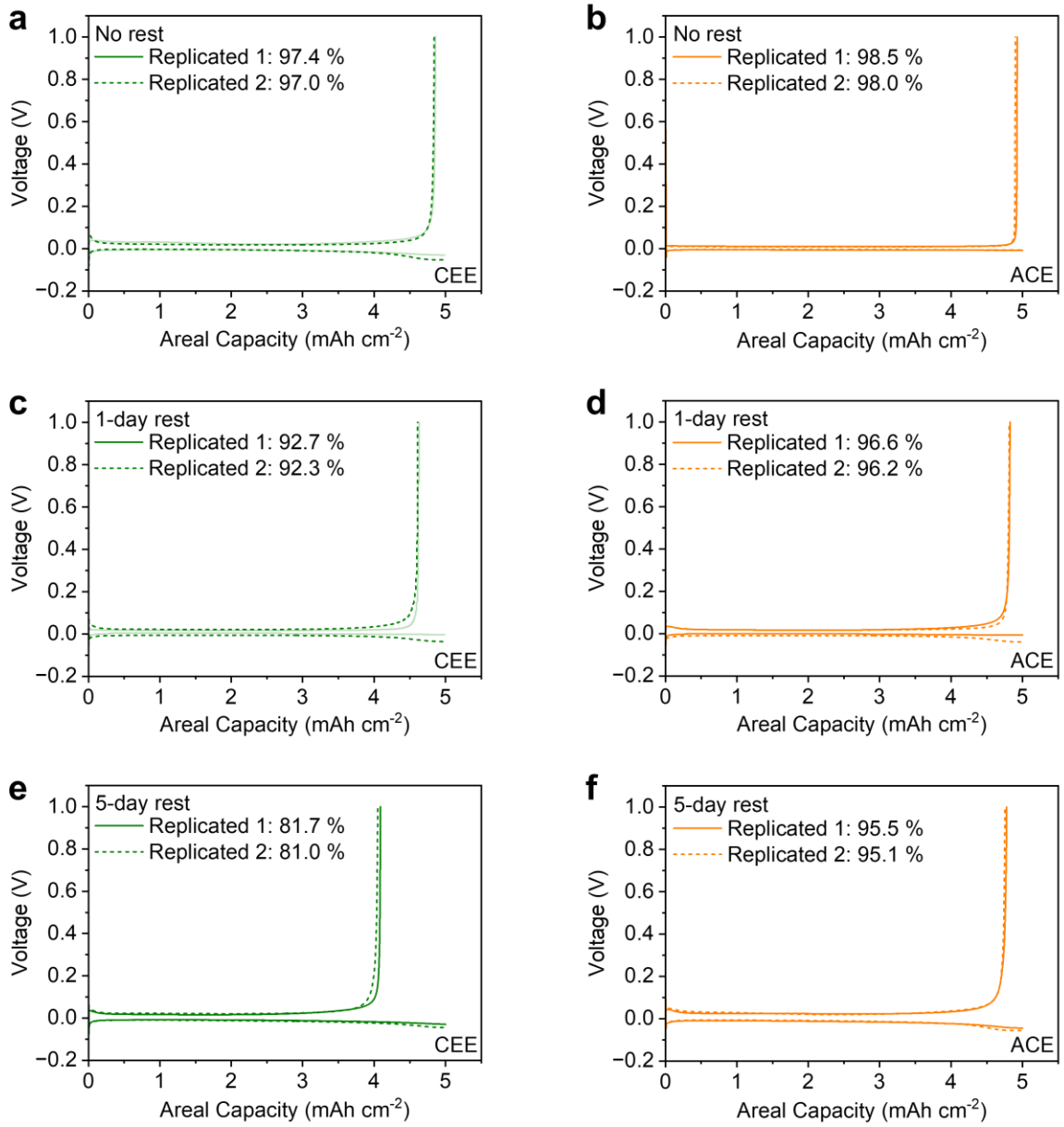

Figure S15. Voltage profiles of the second plating and stripping profiles for (a,c,e) CEE and (b,d,f) ACE. Cells were either (a,b) not rested, (c,d) rested for a day, (e,f) or rested for 5 days.

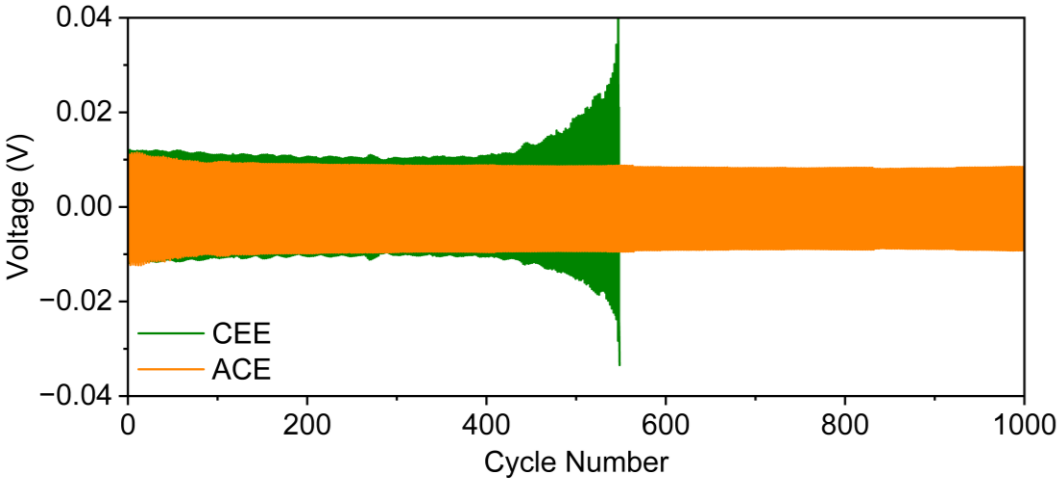

Fig. S16. Cycling stability of Li||Li symmetric cells at 1 mA cm^{-2} and 1 mAh cm^{-2}.

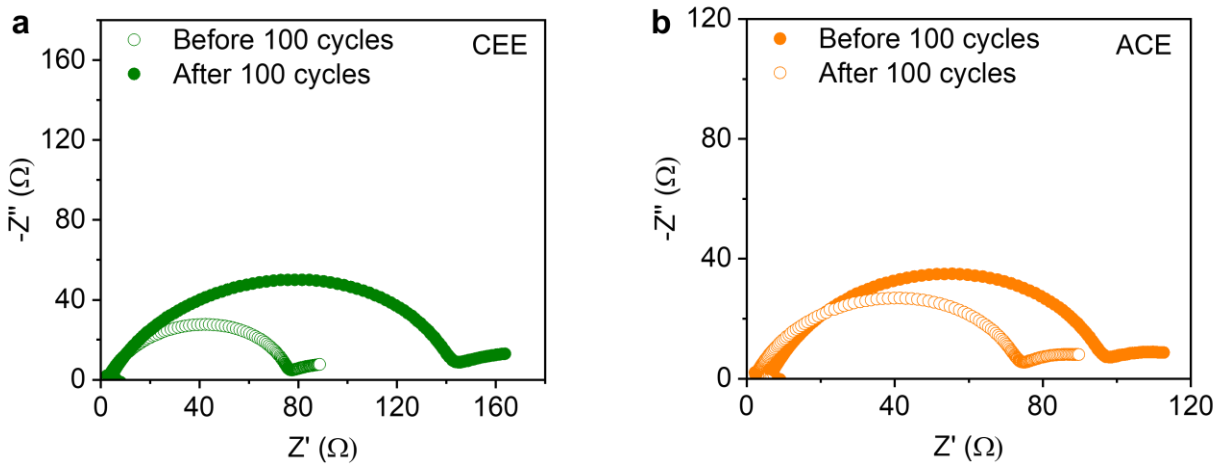

Fig. S17. EIS of Li||Li symmetric cells before and after 100 cycles. (**a**) CEE and (**b**) ACE electrolytes were used to cycle Li||Li symmetric cells for 100 cycles at 1 mA cm^{-2} and 1 mAh cm^{-2}.

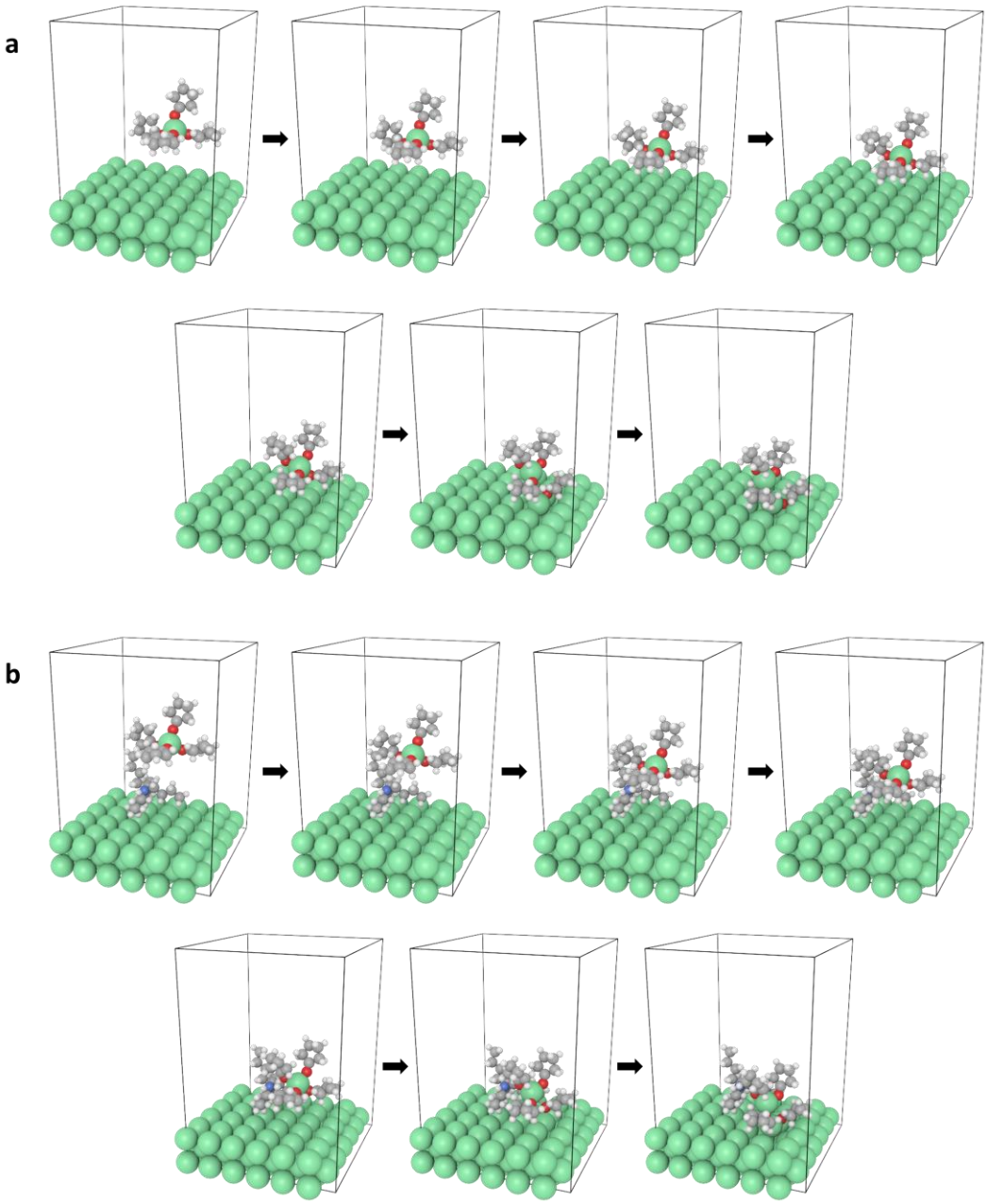

Fig. S18. Snapshots of solvated Li^+ as it progresses towards Li metal anode (**a**) without and (**b**) with TBA^+ cation layer.

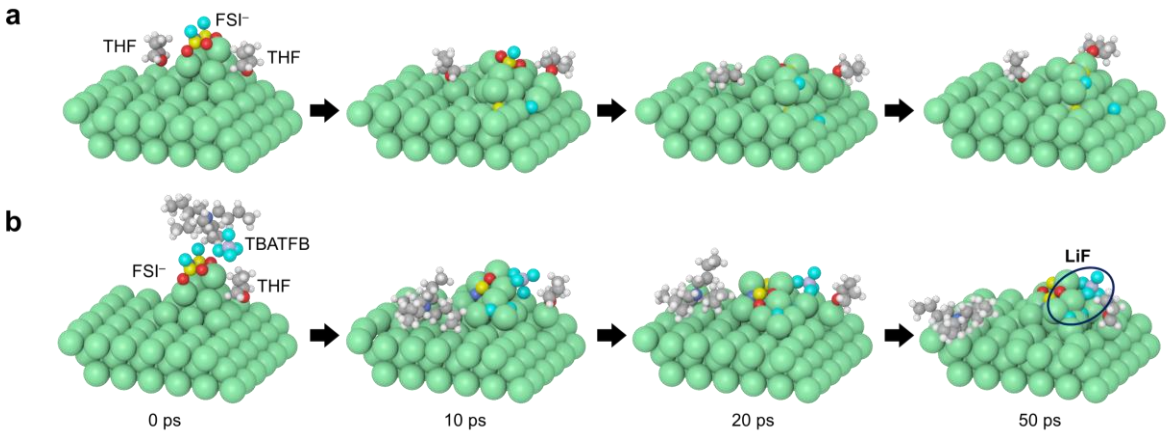

Fig. S19. AIMD simulations of the solvent and salt decomposition process (**a**) without and (**b**) with TBATFB.

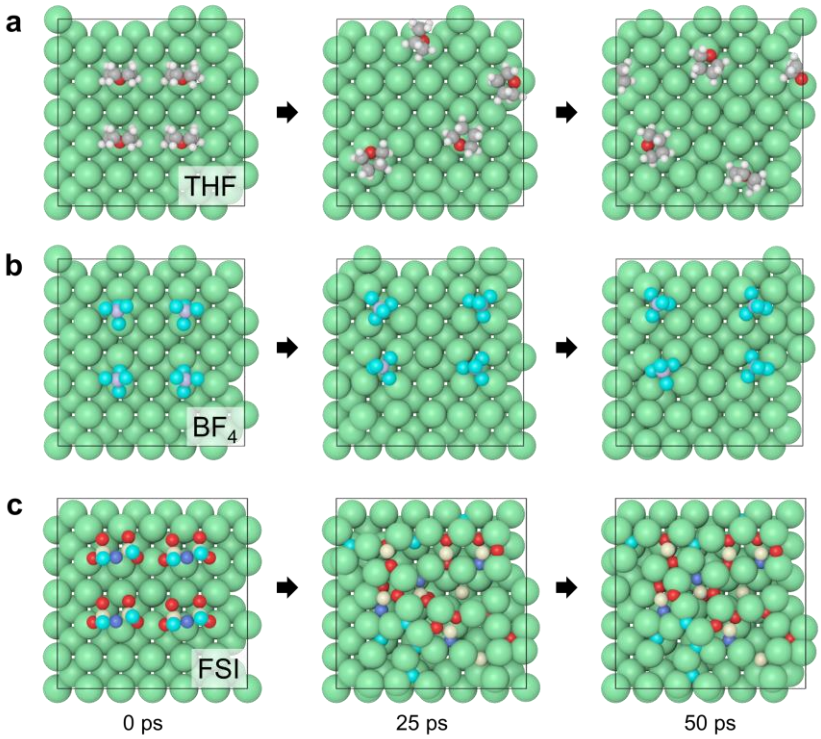

Fig. S20. AIMD simulations of (**a**) THF, (**b**) BF_4^-, and (**c**) FSI^- decomposition process over 50 ps.

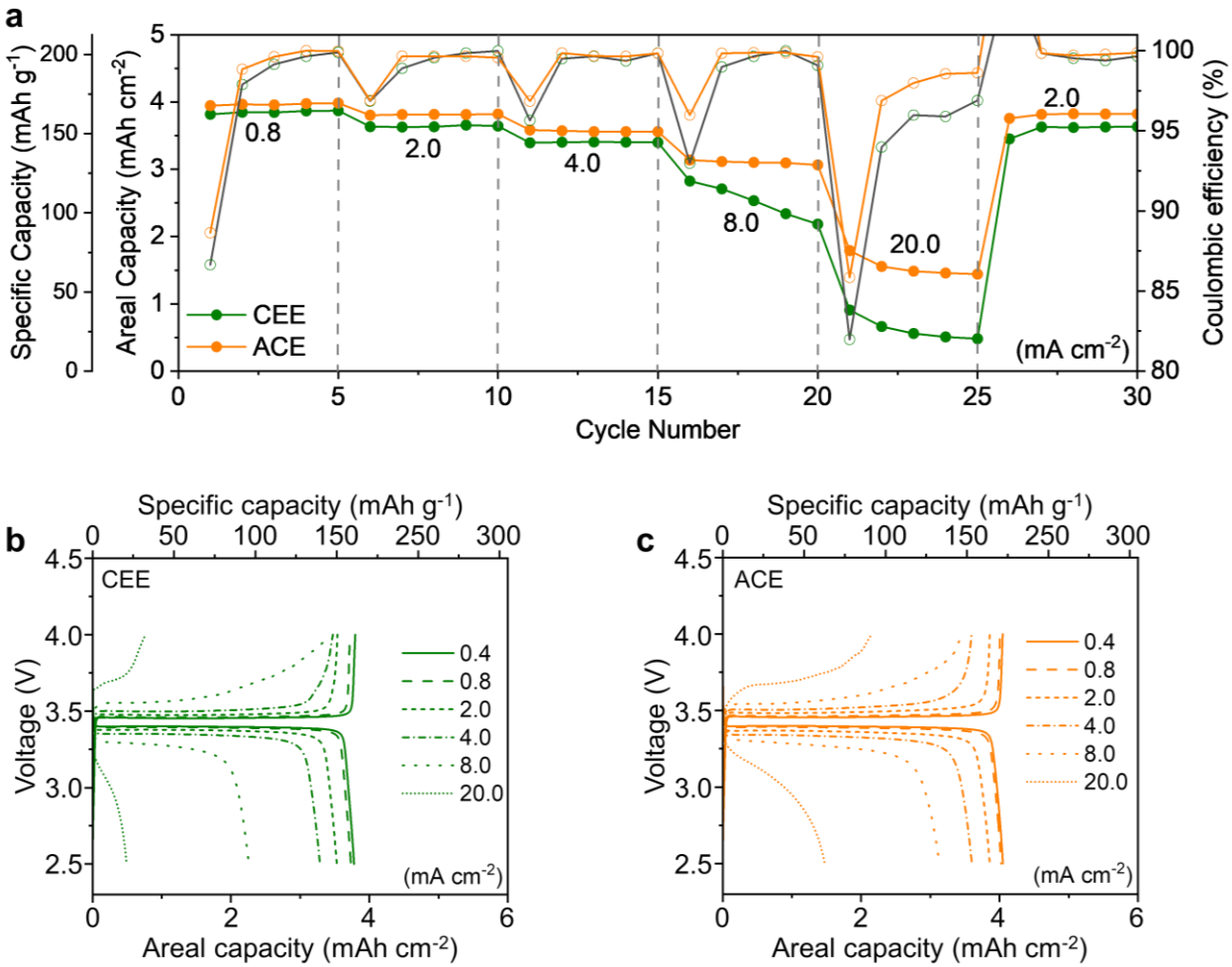

Fig. S21. (**a**) Rate performance of the LFP cathode and (**b** and **c**) corresponding voltage profiles.

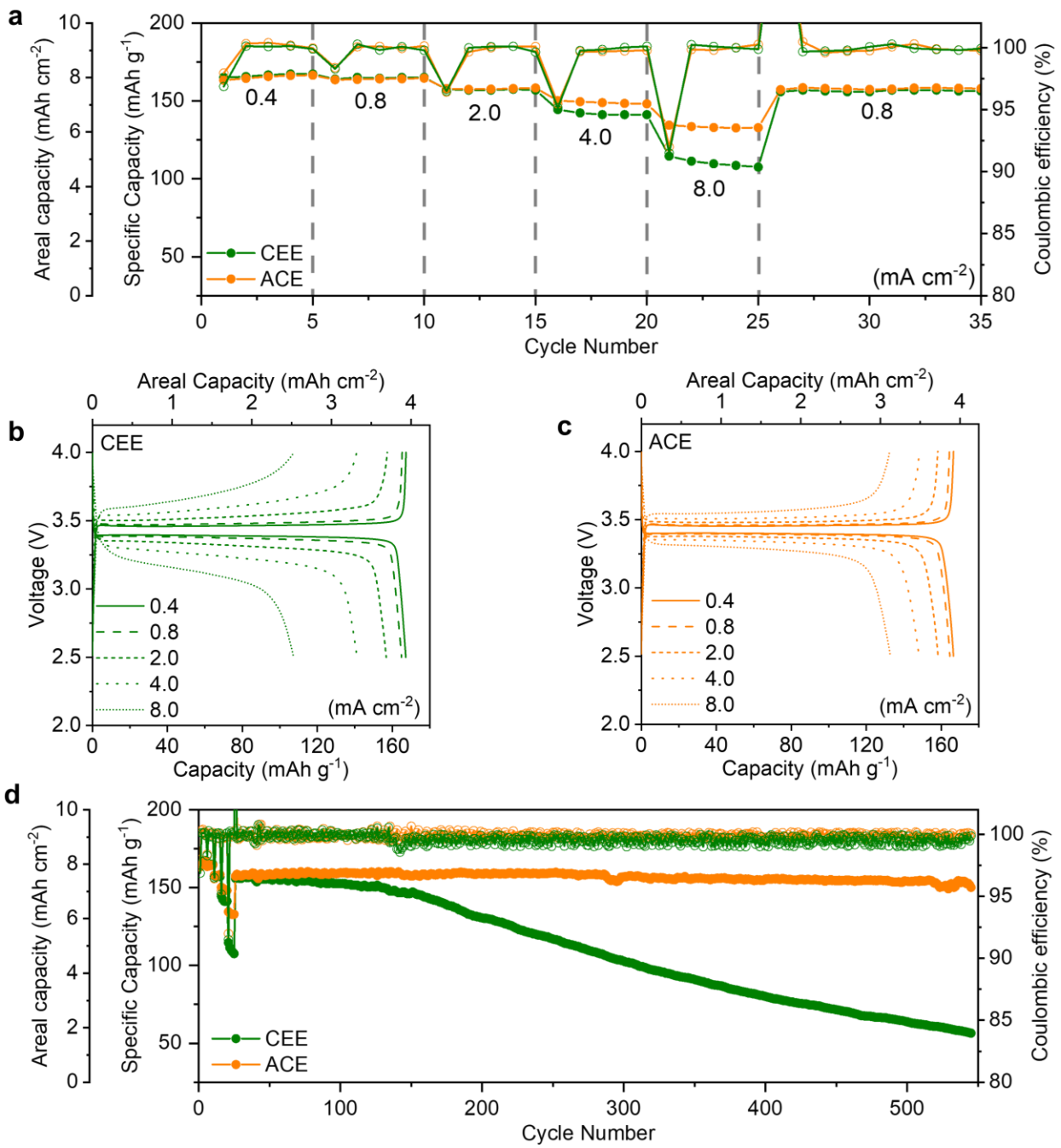

Fig. S22. (**a**) Rate performance of the LFP cathode and (**b** and **c**) corresponding voltage profiles. (**d**) Cycling performance of the LFP cathode at 0.8 mA cm^{-2}.

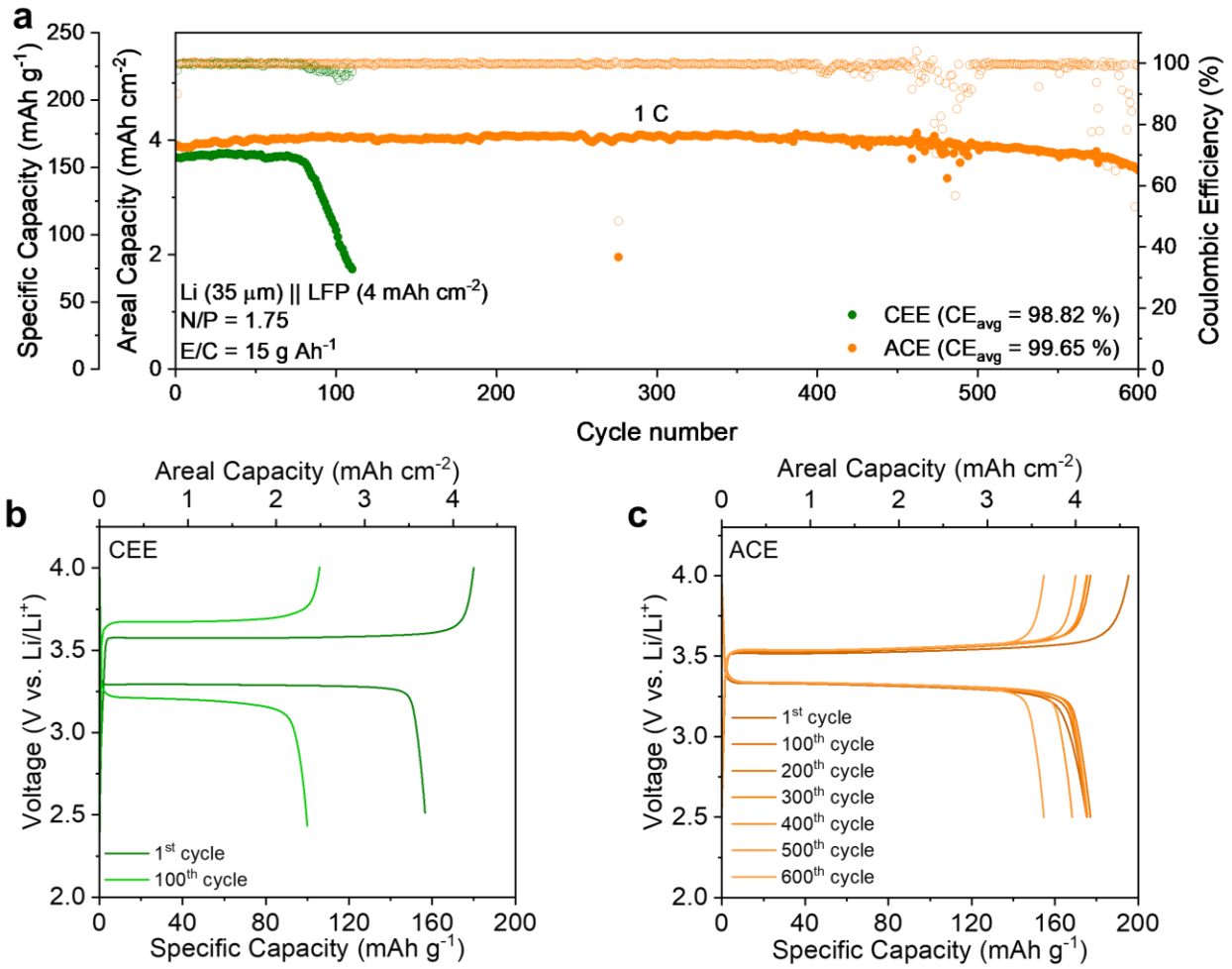

Fig. S23. (**a**) Long-cycling performance of Li||LFP cells and (**b** and **c**) corresponding voltage profiles. Conditions: the 35 µm LMA paired with the 4 mAh cm^{-2} LFP cathode, with N/P ratio of 1.75 and E/C ratio of 15 g Ah^{-1}.

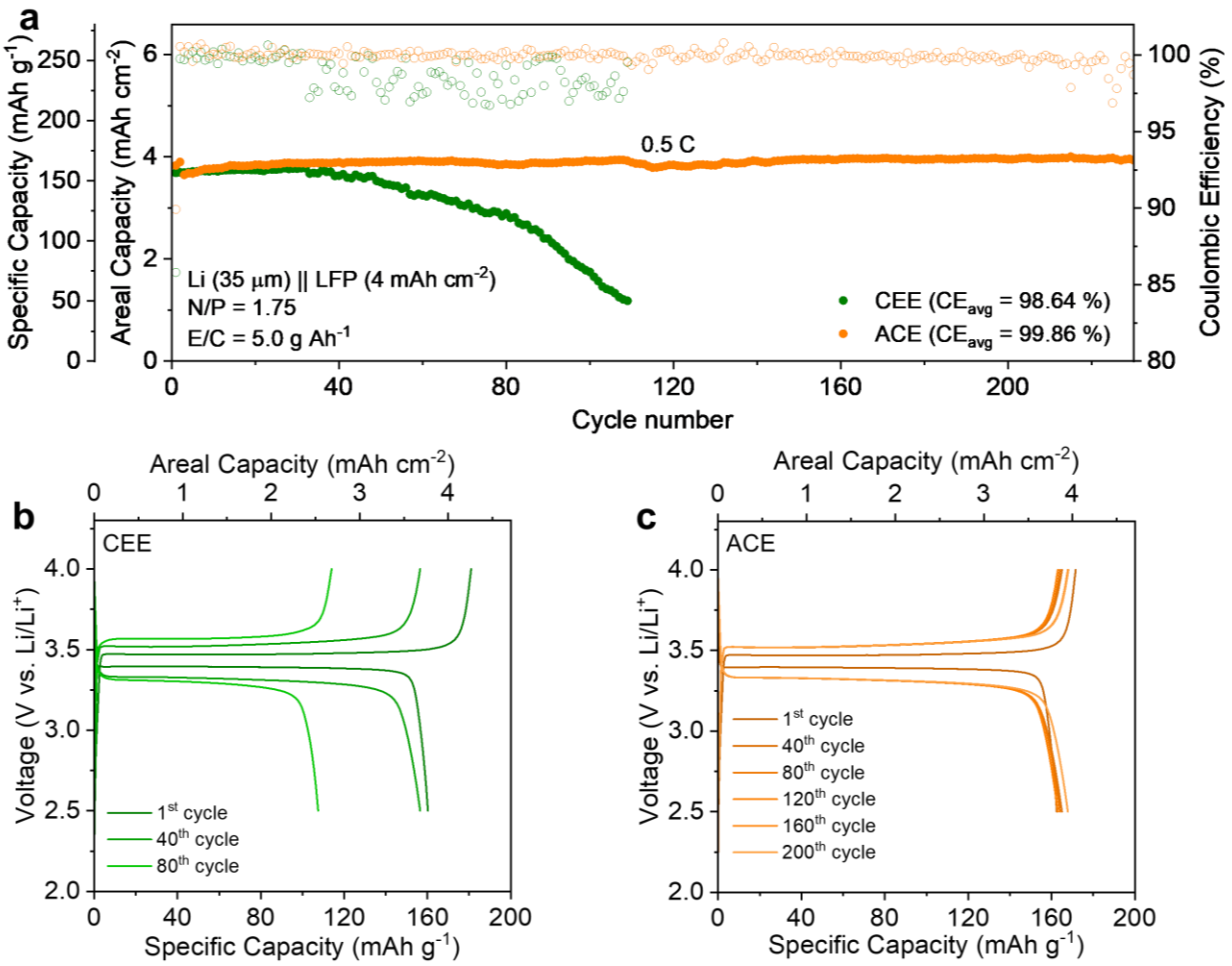

Fig. S24. (**a**) Cycling performance of Li||LFP cells under practical conditions and (**b** and **c**) corresponding voltage profiles. Conditions: the 35 µm LMA paired with the 4 mAh cm^{-2} LFP cathode, with N/P ratio of 1.75 and E/C ratio of 5 g Ah^{-1}.

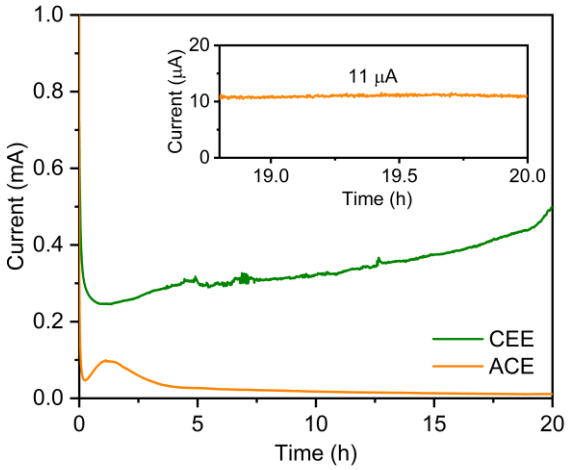

Fig. S25. Electrochemical floating test of Li||NCA88 cells at 4.3 V vs. Li/Li^+ for 20 hours.

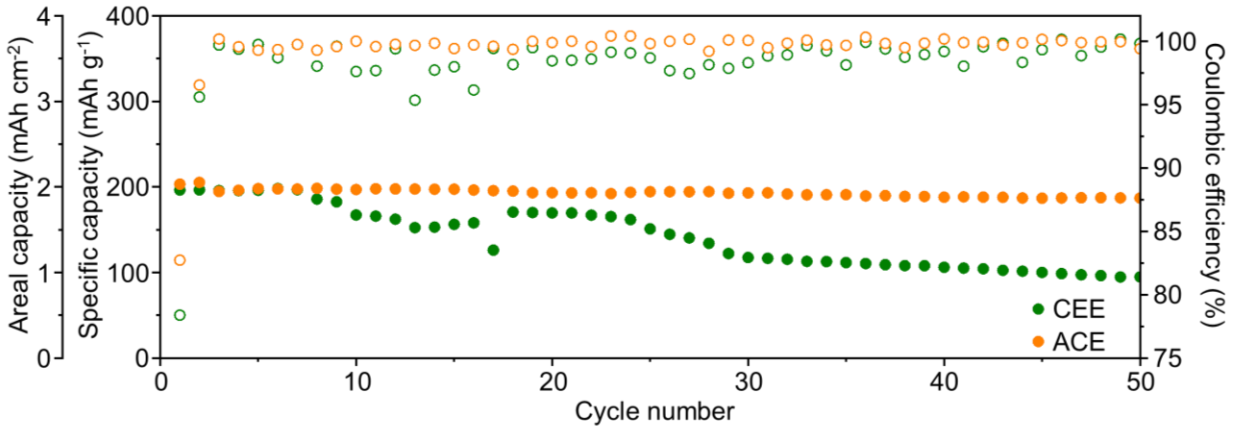

Fig. S26. Capacity of the NCA88 cathodes (2 mAh cm^{-2}) cycled at 1 C.

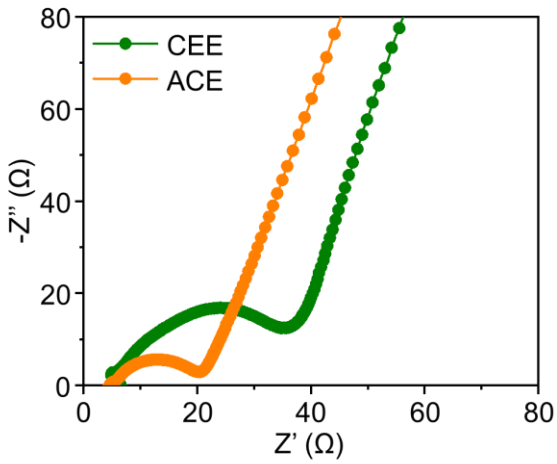

Fig. S27. EIS profiles of the cycled NCA88 cathodes

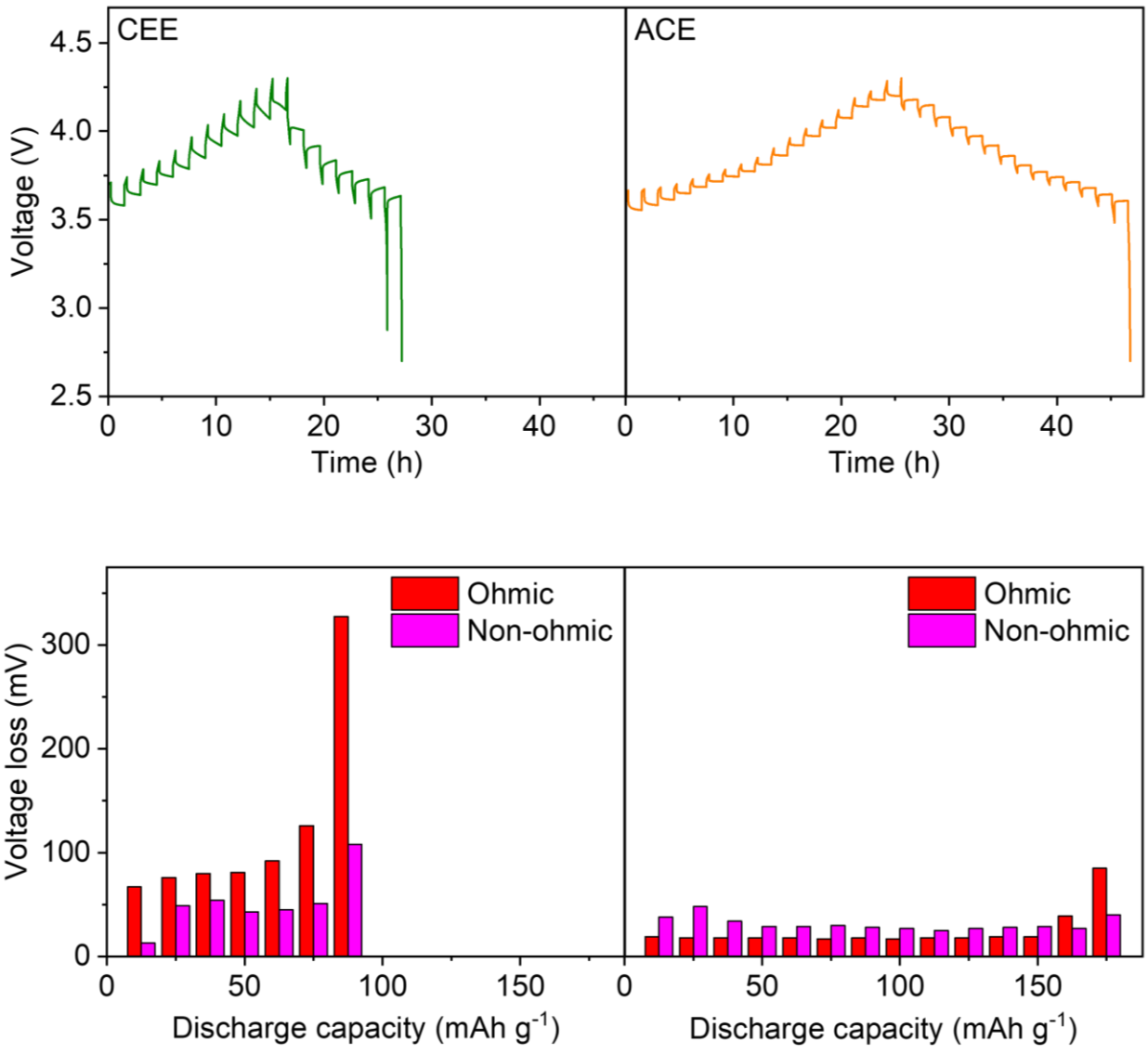

Fig. S28. Voltage-time profiles of GITT of cycled Li||NCA88 cells using CEE and ACE. Ohmic and non-ohmic voltage loss measured from GITT profiles as a function of discharge capacity.

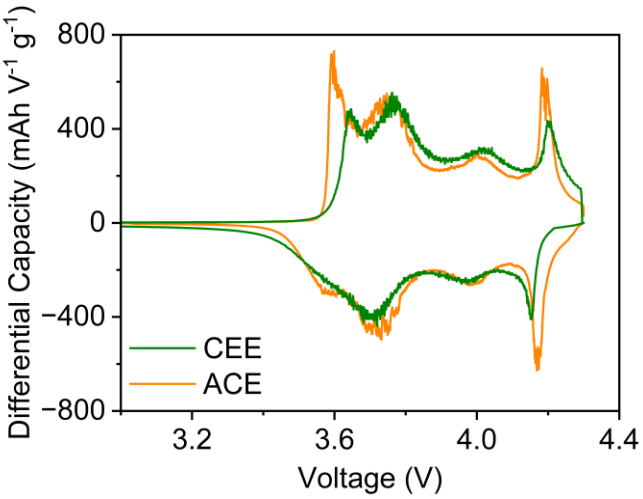

Fig. S29. Differential capacity as a function of voltage (dQ dV^{-1} vs. V) of Li||NCA88 measured between 3.0 and 4.3 V.

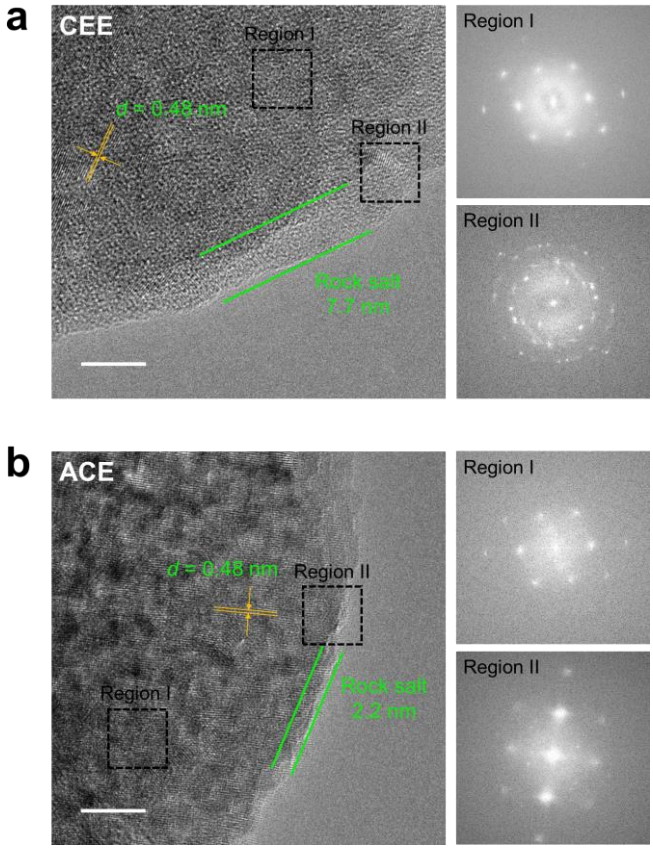

Fig. S30. Transmission electron microscopy images and Fourier transform of the NCA88 cathodes cycled in (a) CEE and (b) ACE. Scale bar 5 nm

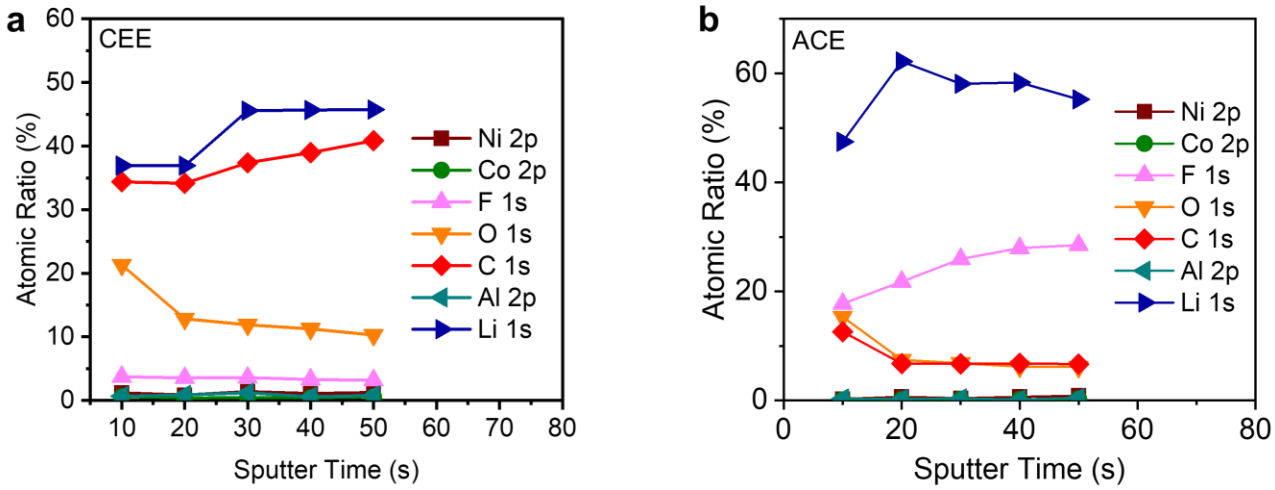

Fig. S31. Atomic composition ratios at different sputtering times using (**a**) CEE and (b) ACE.

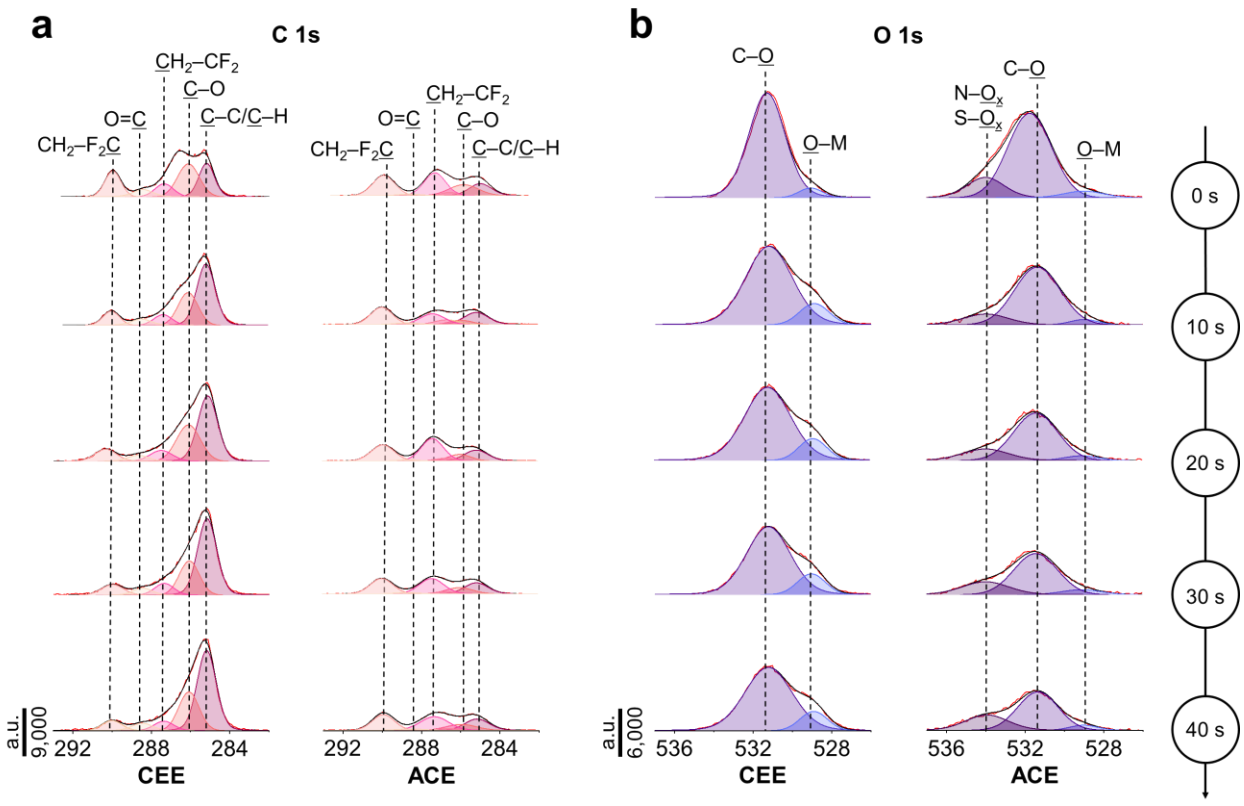

Fig. S32. XPS characterization of cycled NCA88. (a) C 1s and (b) O 1s spectra of CEE- and ACE-cycled NCA88 are displayed on columns, with each heigh corresponding to depth profiling results.

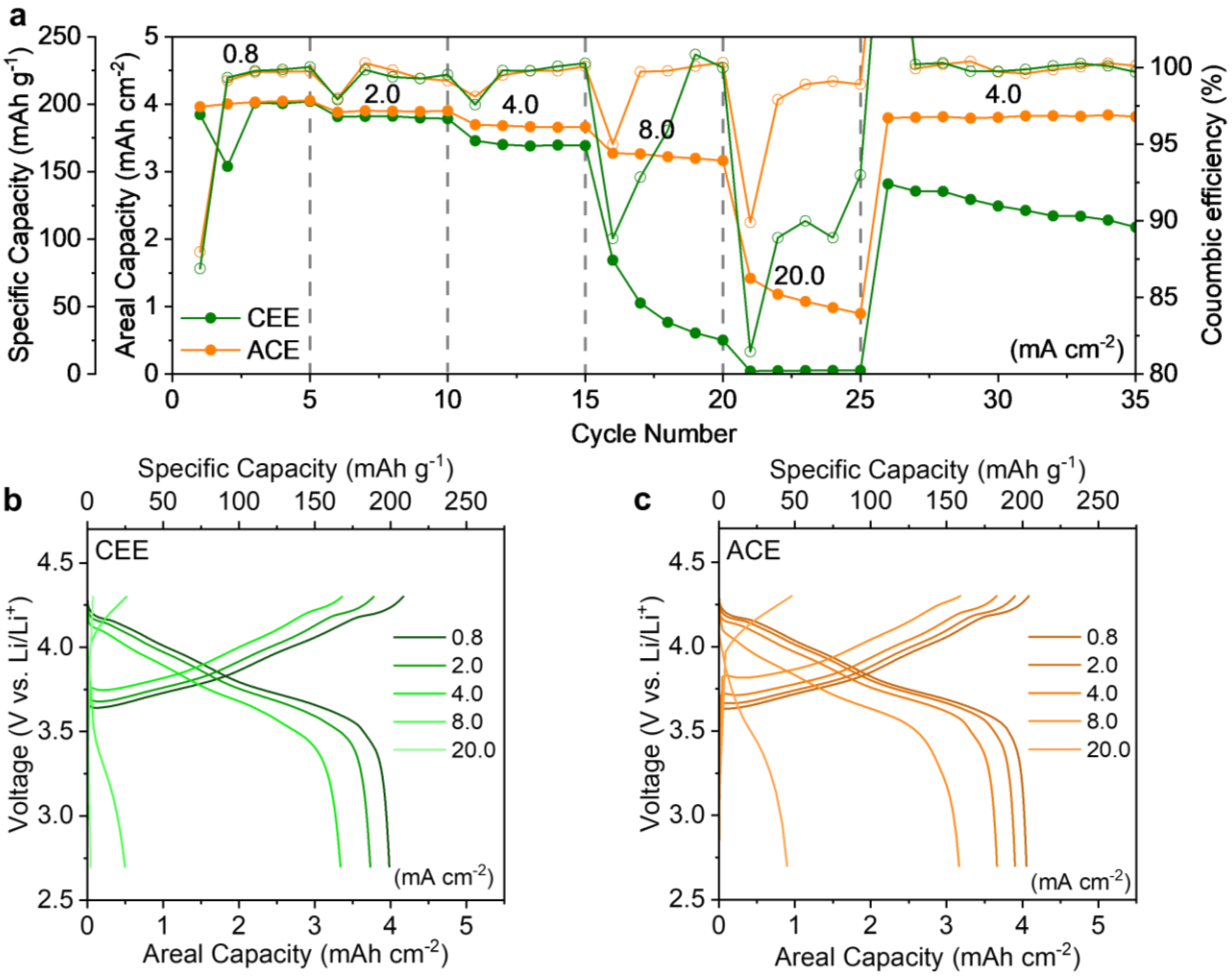

Fig. S33. (**a**) Rate performance of the NCA88 cathode and (**b** and **c**) corresponding voltage profiles.

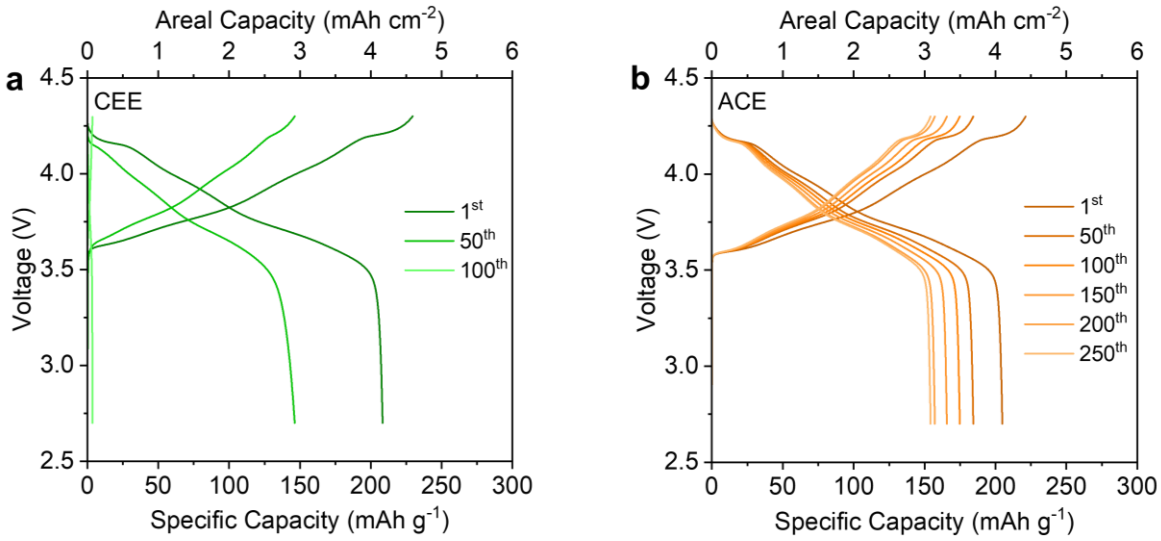

Fig. S34. Voltage profiles of long-term cycling of Li||NCA88 cells using (**a**) CEE and (**b**) ACE. Conditions: 50 µm LMA paired with 2 mAh cm^{-2} NCA88 cathode, with N/P ratio of 5.0 and E/C ratio of 10.2 g Ah^{-1}.

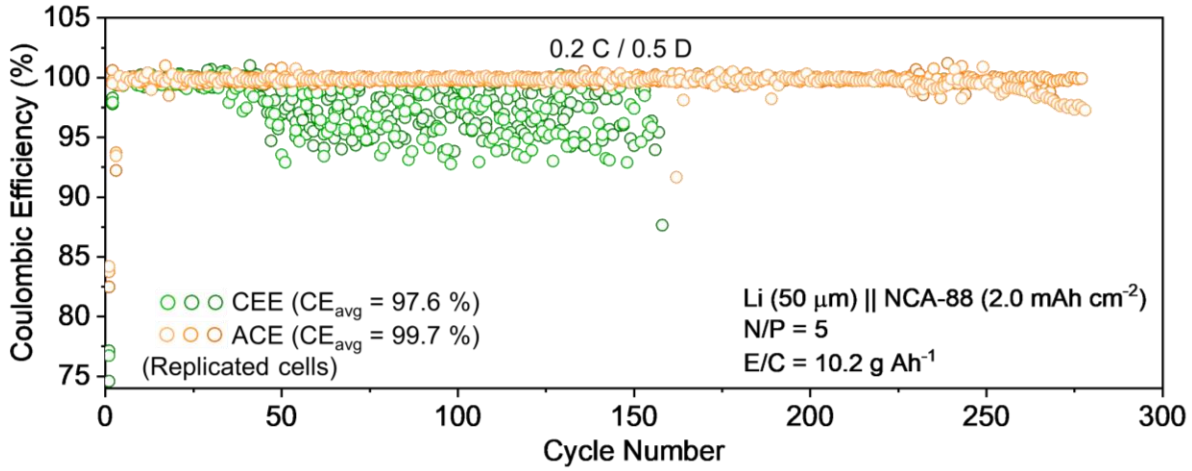

Fig. S35. CE of Li||NCA88 cycling performances. Conditions: 50 µm LMA paired with 2 mAh cm^{-2} NCA88 cathode, with N/P ratio of 5.0 and E/C ratio of 10.2 g Ah^{-1}.

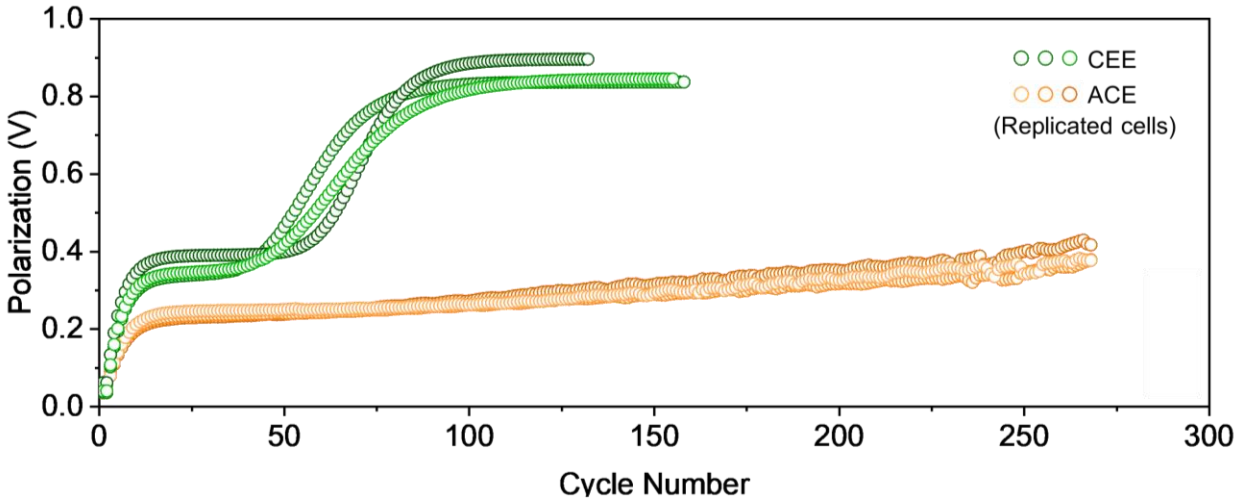

Fig. S36. Voltage polarization of Li||NCA88 cycling performances. Conditions: the 50 μm LMA paired with the 2 mAh cm^{-2} NCA88 cathode, with N/P ratio of 5.0 and E/C ratio of 10.2 g Ah^{-1}.

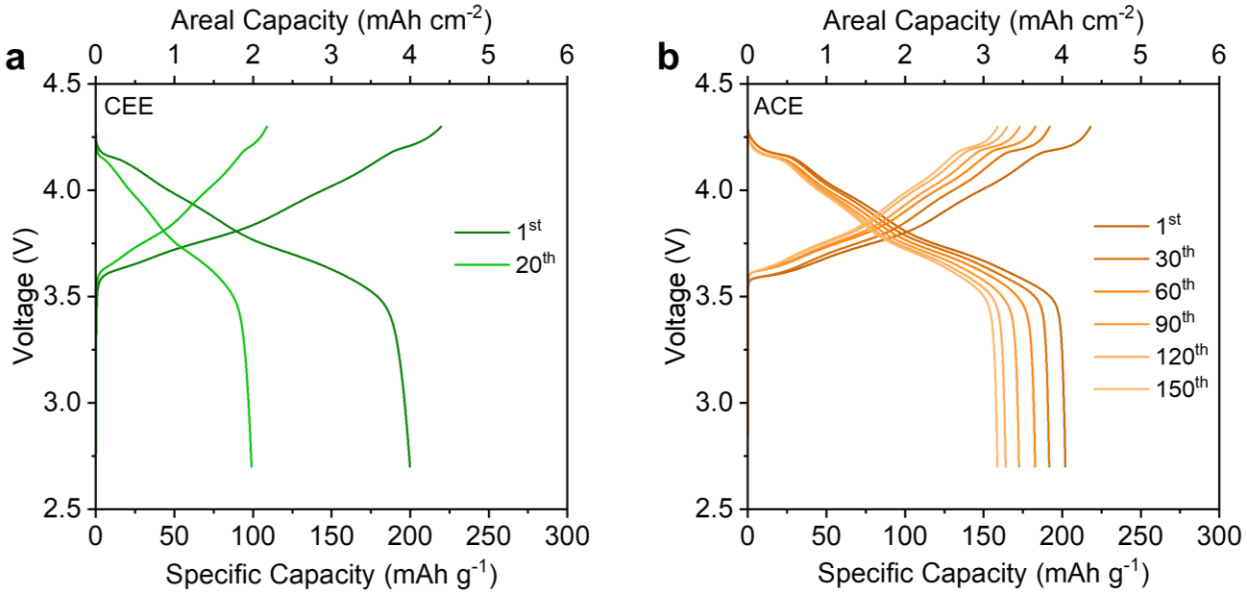

Fig. S37. Voltage profiles of long-term cycling of Li||NCA88 cells using (**a**) CEE and (**b**) ACE. Conditions: the 35 µm LMA paired with the 4 mAh cm^{-2} NCA88 cathode, with N/P ratio of 1.75 and E/C ratio of 5.1 g Ah^{-1}.

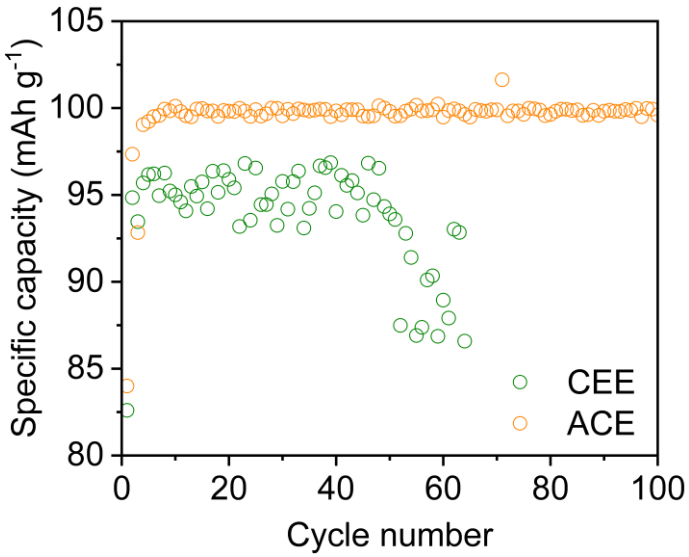

Fig. S38. CE of Cu||NCA88 cycling performances. Conditions: Cu paired with the 2 mAh cm^{-2} NCA88 cathode, with E/C ratio of 5.1 g Ah^{-1}.

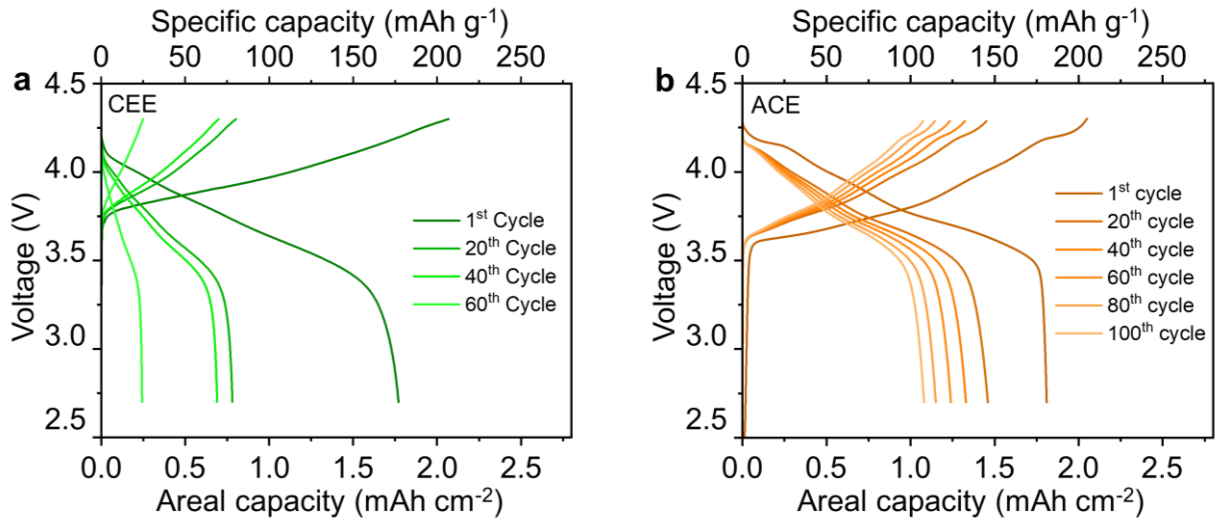

Fig. S39. Voltage profiles of Cu||NCA88 cycling performances. Conditions: Cu paired with the 2 mAh cm^{-2} NCA88 cathode, with E/C ratio of 5.1 g Ah^{-1}.

Table S1. Physiochemical properties and normalized cost of different solvents and diluents

Solvent/Diluent	Molecular Weight (g mol^{-1})	Density (kg m^{-3})	Normalized Price (USD L^{-1})
1,2-Dimethoxyethane (DME)	90.12	868	113
Diethyl ether (DEE)	74.12	713	128
Sulfolane (SL) / Tetramethylene sulfone (TMS)	120.17	1260	100.4
Triethyl phosphite (TEP)	166.16	969	53.25
Dimethyl carbonate (DMC)	90.08	1070	101
Bis(2,2,2-trifluoroethyl) ether (BTFE)	182.06	1404	22600
1,1,2,2-Tetrafluoroethyl 2,2,3,3-tetrafluoropropyl ether (TTE)	232.07	1533	2855.2
Tris(2,2,2-trifluoroethyl)orthoformate (TFEO)	310.12	1457	39800
2,2,3,3-tetrafluoro-1,4-dimethoxybutane (FDMB)	190.14	980	27200
Fluoroethylene carbonate (FEC)	106.05	1454	15860
Methyl (2,2,2-trifluoroethyl) carbonate (FEMC)	158.08	1340	9000
Tetrahydrofuran (THF)	72.11	888	20.34
1,1,2,2-Tetrafluoroethyl 2,2,2-trifluoroethyl ether (HFE)	200.05	1487	3000

N,N-Dimethylsulfamoyl fluoride (FSA)	127.14	1334	58100
N,N-Dimethyltrifluoromethanesulfonamide (DMTMFSA)	177.15	1374	17900
1,2-Bis(2,2-difluoroethoxy)ethane (F4DEE)	190.14	1240	77600
Ethylene carbonate (EC)	88.06	1321	49
1,3-Dioxolane (DOL)	74.08	1060	191
2-Methyltetrahydrofuran (MeTHF)	86.13	854	145
2,5-Dimethyltetrahydrofuran (DMeTHF)	100.16	833	8760
Dimethoxymethane (DMM)	76.09	860	216

Table S2. Physiochemical properties and normalized cost of different salts

Solvent/Diluent	Molecular Weight ($g\ mol^{-1}$)	Density ($kg\ m^{-3}$)	Normalized Price ($USD\ kg^{-1}$)
Lithium Bis(fluorosulfonyl)imide (LiFSI)	187.07	1052	6780
Lithium Hexafluorophosphate ($LiPF_6$)	151.91	1500	4700
Lithium Bis-trifluoromethanesulfonimide (LiTFSI)	287.07	1333	5180
Lithium difluoro(oxalato)borate (LiDFOB)	143.77	2120	4780
Lithium nitrate ($LiNO_3$)	68.95	2380	1640
Tetrabutylammonium tetrafluoroborate (TBATFB)	329.27	1036	2580

Table S3. Comparison of the state-of-the-art Li||Cu coulombic efficiencies

Comparison Reference	Electrolyte	Li||Cu Coulombic Efficiency (%)	Current density (mA cm^{-2})	Capacity (mAh cm^{-2})	Electrolyte Cost (USD L^{-1})
S1	1 M LiFSI DEE[6]	99.0	0.5	1	1400.60
S2	0.5 M LiFSI + 0.5 M LiTFSI DME:DOL (1:1)[7]	99.0	0.25	0.625	1531.89
S3	1 M LiTFSI DME:DOL (1:1) + 3 wt% $LiNO_3$[8]	98.5	0.5	1	1673.07
S4	4 M LiFSI DEE[9]	99.38	0.5	1	5218.42
S5	4 M LiFSI DME[9]	99.04	0.5	1	5203.42
S6	3.85 M LiFSI THF[10]	98.5	1	2	4919.87
S7	1 M LiFSI DME:FDMH (1:6)[11]	99.4	0.5	1	24604.59
S8	LiFSI:DME:TTE (1:1.2:3)[12]	99.3	0.5	1	4508.50
S9	1 M LiFSI DMeTHF[13]	98.4	1	1	10032.61
S10	1 M LiFSI MeTHF[13]	98.2	1	1	1417.61
S11	1 M LiFSI + 1 M LiTFSI DOL:DME (1:4) + 0.02 M KPBS[14]	99.1	1	1	2911.78
S12	2 M LiFSI + 1 M LiTFSI DOL:DME (1:1) + 3 wt% $LiNO_3$[15]	98.5	0.5	1	4398.96

S13	1 M LiFSI FDMB[16]	99.2	0.25	0.5	28472.61
S14	4.86 M LiFSI THF[17]	99.3	1	1	6205.20
S15	2.43 M LiFSI THF:TTE (1:1)[17]	99.4	1	1	4530.20
S16	1.5 M LiFSI DME[18]	96.7	0.5	0.5	2021.91
S17	1.5 M LiFSI DMM[18]	99.1	0.5	0.5	2124.91
S18	3 M LiFSI DME[19]	99	0.5	1	3930.82
S19	1.2 M LiFSI F4DEE[20]	99.74	0.5	1	79127.13
This work	**1 M LiFSI + 0.1 M TBATFB THF**	**99.4**	**1**	**1**	**1377.894**
This work	**1 M LiFSI + 0.1 M TBATFB THF**	**99.2**	**3**	**3**	**1377.894**

Table S4. Comparison of the state-of-the-art Li metal battery performances.

Comparison Reference	Electrolyte	Cycle number	Capacity retention	E/C ratio	N/P ratio	Practicality factor	Electrolyte Cost (USD L^{-1})
4	1 M LiFSI DEE[6]	182	80	8	2	16	5218.42
5	0.5 M LiFSI + 0.5 M LiTFSI DME:DOL (1:1)[7]	94	80	8	2	16	5203.42
7	1 M LiFSI DME:FDMH (1:6)[11]	250	76	10	2	20	24604.59
8	LiFSI:DME:TTE (1:1.2:3)[12]	155	80	3	2.48	7.44	4508.50
19	1.2 M LiFSI F4DEE[20]	200	80	8	2.125	17	79127.13
20	LiFSI:THF:TTE (1:2.6:3.2)[21]	160	80.7	37.5	45	1687.5	3560.83
This work	**1 M LiFSI + 0.1 M TBATFB THF**	**150**	**82.4**	**5.1**	**1.75**	**8.925**	**1377.89**
This work	**1 M LiFSI + 0.1 M TBATFB THF**	**250**	**79.4**	**4**	**5**	**20**	**1377.89**

References

1. G. Kresse and J. Hafner, *Phys. Rev. B Condens. Matter*, 1993, **47**, 558-561.

2. G. Kresse and J. Furthmuller, *Phys. Rev. B*, 1996, **54**, 11169-11186.

3. P. E. Blochl, *Phys. Rev. B*, 1994, **50**, 17953-17979.

4. J. P. Perdew, K. Burke and M. Ernzerhof, *Phys. Rev. Lett.*, 1996, **77**, 3865-3868.

5. C. Chen and S. P. Ong, *Nat. Comput. Sci.*, 2022, **2**, 718-728.

6. J. Holoubek, H. Liu, Z. Wu, Y. Yin, X. Xing, G. Cai, S. Yu, H. Zhou, T. A. Pascal, Z. Chen and P. Liu, *Nat. Energy*, 2021, **6**, 303-313.

7. R. R. Miao, J. Yang, X. J. Feng, H. Jia, J. L. Wang and Y. N. Nuli, *J. Power Sources*, 2014, **271**, 291-297.

8. S. Y. Yuan, S. T. Weng, F. Wang, X. L. Dong, Y. G. Wang, Z. X. Wang, C. Shen, J. L. Bao, X. F. Wang and Y. Y. Xia, *Nano Energy*, 2021, **83**, 105847.

9. Y. L. Chen, Z. Yu, P. Rudnicki, H. X. Gong, Z. J. Huang, S. C. Kim, J. C. Lai, X. Kong, J. Qin, Y. Cui and Z. N. Bao, *J. Am. Chem. Soc.*, 2021, **143**, 18703-18713.

10. T. D. Pham, A. Bin Faheem and K. K. Lee, *Small*, 2021, **17**, 2103375.

11. H. Wang, Z. Yu, X. Kong, W. Huang, Z. Zhang, D. G. Mackanic, X. Huang, J. Qin, Z. Bao and Y. Cui, *Adv. Mater.*, 2021, **33**, 2008619.

12. X. Ren, L. Zou, X. Cao, M. H. Engelhard, W. Liu, S. D. Burton, H. Lee, C. Niu, B. E. Matthews, Z. Zhu, C. Wang, B. W. Arey, J. Xiao, J. Liu, J-G. Zhang and W. Xu, *Joule*, 2019, **3**, 1662-1676.

13. R. Xu, J. F. Ding, X. X. Ma, C. Yan, Y. X. Yao and J. Q. Huang, *Adv. Mater.*, 2021, **33**, 2105962.

14. D. D. Wang, H. D. Liu, M. Q. Li, D. W. Xia, J. Holoubek, Z. Deng, M. Y. Yu, J. H. Tian, Z. Q. Shan, S. P. Ong, P. Liu and Z. Chen, *Nano Energy*, 2020, **75**, 104889.

15. F. L. Qiu, X. Li, H. Deng, D. Wang, X. W. Mu, P. He and H. S. Zhou, *Adv. Energy Mater.*, 2019, **9**, 1803372.

16. Z. Yu, H. Wang, X. Kong, W. Huang, Y. Tsao, D. G. Mackanic, K. C. Wang, X. Wang, W. Huang, S. Choudhury, Y. Zheng, C. V. Amanchukwu, S. T. Hung, Y. Ma, E. G. Lomeli, J. Qin, Y. Cui and Z. Bao, *Nat. Energy*, 2020, **5**, 526-533.

17. T. Chen, J. You, R. Li, H. Li, Y. Wang, C. Wu, Y. Sun, L. Yang, Z. Ye, B. Zhong, Z. Wu and X. Guo, *Adv. Sci.*, 2022, **9**, 2203216.

18. S. Ko, T. Obukata, T. Shimada, N. Takenaka, M. Nakayama, A. Yamada and Y. Yamada, *Nat. Energy*, 2022, **7**, 1217-1224.

19. J. Moon, D. O. Kim, L. Bekaert, M. Song, J. Chung, D. Lee, A. Hubin and J. Lim, *Nat. Commun.*, 2022, **13**, 4538.

20. Z. Yu, P. E. Rudnicki, Z. Zhang, Z. Huang, H. Celik, S. T. Oyakhire, Y. Chen, X. Kong, S. C. Kim, X. Xiao, H. Wang, Y. Zheng, G. A. Kamat, M. S. Kim, S. F. Bent, J. Qin, Y. Cui and Z. Bao, *Nat. Energy*, 2022, **7**, 94-106.

21. Y. Lin, Z. Yang, X. Zhang, Y. Liu, G. Hu, S. Chen and Y. Zhang, *Energy Storage Mater.*, 2023, **58**, 184-194.